Progress In Electromagnetics Research C, Vol. 173, 180–189, 2026 PIER C

(Received 26 June 2026, Accepted 1 August 2026, Scheduled 8 September 2026)

A Four-Port Wideband MIMO Antenna with Tapered Feedline and U-Shaped Slots for Dual-Band Rejection and Circular Polarization

Pandillapalli Janardhana Reddy[1,*] and Gummadi Kameswari[2]

[1] *Department of ECE, RGUKT A.P R K Valley, Research Scholar JNTUA, A.P, India*
[2] *Department of ECE, NBKR Institute of Science and Technology, Nellore, A.P, India*

ABSTRACT: This work presents a compact four-port low-profile multi-input multi-output (MIMO) antenna designed for wideband wireless communication over the S- (2–4 GHz), C- (4–8 GHz), and lower X-band (8–12 GHz) spectrum. The proposed antenna initially exhibits a broad impedance bandwidth extending from 2.5 to 9 GHz under the standard -10 dB matching condition. To improve spectral selectivity and mitigate unwanted interference, U-shaped slots are embedded in the feeding line and radiator, generating two distinct rejection bands at 3.5–3.9 GHz and 5.1–5.9 GHz, corresponding to WiMAX and WLAN frequencies, respectively. Including these slots slightly shifts the upper operating limit to 8.5 GHz. Implemented on an FR4 dielectric substrate ($\varepsilon_r = 4.4$) with a thickness of 1.6 mm, the antenna occupies an overall footprint of $40 \times 34\,\text{mm}^2$. Additionally, circular polarization is achieved across the 6.1–7.9 GHz region, enhancing communication reliability in multipath propagation environments. A common-ground decoupling structure is employed to improve port isolation and suppress mutual coupling, resulting in isolation greater than 20 dB. The antenna demonstrates favorable diversity characteristics, with an envelope correlation coefficient below 0.05 and a diversity gain exceeding 9.95 dB. Moreover, a maximum realized gain of 6.2 dBi is obtained within the operational band. Experimental validation of the fabricated prototype confirms close agreement with simulated results, highlighting its potential for compact wideband multi-antenna wireless systems.

1. INTRODUCTION

Ultra-wideband (UWB) communication has gained significant attention for modern wireless applications owing to its capability to support high-speed data transmission over short distances. Owing to their compact size, low power spectral density, high temporal resolution, and broad operating bandwidth, UWB antennas have found extensive applications in imaging systems, radar, biomedical sensing, and high-speed wireless communications [1, 2].

Despite these advantages, UWB systems face several challenges, including limited communication range, multipath fading, high mutual coupling in antenna arrays, and difficulties in broadband impedance matching. To overcome these limitations, MIMO technology has been widely integrated with UWB antennas, offering improved channel capacity, enhanced spatial diversity, reduced multipath effects, lower mutual coupling, and improved system reliability [3, 4].

Several UWB antenna designs have been reported to enhance antenna performance. A coplanar waveguide (CPW)-fed UWB antenna integrated with a voltage doubler rectifier circuit for operation over 2.16–6.32 GHz was presented in [5]. In [6], a folded dipole antenna structure achieved omnidirectional radiation characteristics with a gain varying from 0.8 to 6 dBi. Half-loop monopole radiators combined with interconnected parasitic elements were utilized in [7] to improve radiation gain. In [8], meandered monopole elements integrated with L-shaped parasitic structures and short stubs enhanced the bandwidth of a compact UWB-MIMO antenna. In [9], carbon black film was employed to enhance isolation by absorbing inter-element interference, while a compact quarter-loop and a circular planar monopole achieved pattern diversity and high isolation [10]. In [11], the antenna compactness is realized via a staircase U-shaped radiating structure, and an I-shaped decoupling stub incorporating rectangular strips is used to suppress mutual coupling.

Although UWB systems provide wide operational bandwidth, interference from coexisting wireless services, such as WiMAX, WLAN, and X-band satellite communications, significantly affects their performance. Therefore, integrating band-notch characteristics into UWB antennas is essential to suppress unwanted frequency bands. In [12], the notch frequency is reconfigured between 5.4 GHz and 3.5 GHz by loading band-stop resonators. A vertex-fed octagonal ring integrated with a split-ring resonator (SRR) and a reconfigurable inclined L-shaped slotted ground plane realizes six wireless frequency bands in [13]. In [14], multiband operation is achieved by integrating a fractal radiating element with an SRR metamaterial structure and a partially slotted rectangular ground plane. Dual-band rejection is realized using U-shaped and inverted U-shaped slot structures in a circular radiating element [15]. A spiral resonator adjacent to a feed line produces both WiMAX

* Corresponding author: Pandillapalli J. Reddy (janardhanareddypandillapalli@gmail.com).

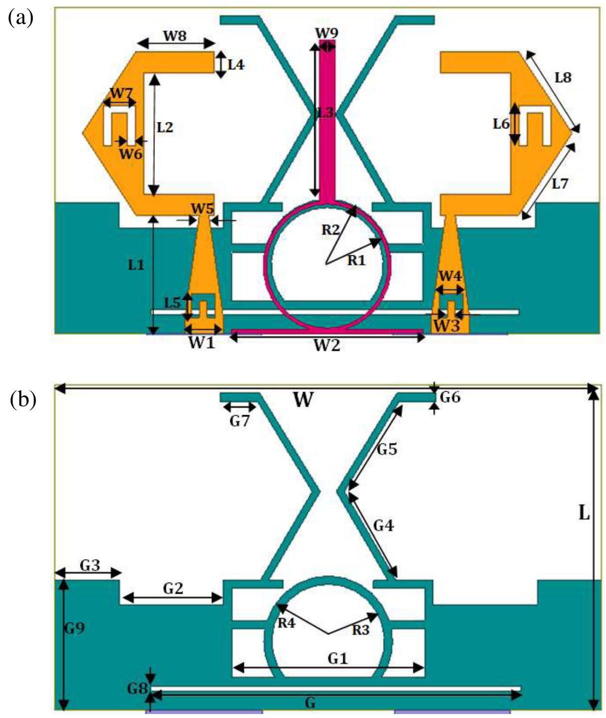

FIGURE 1. Proposed antenna. (a) Top surface and (b) bottom surface.

and X-band notches through a single compact structure in [16]. A T-shaped stub and slot were employed in [17] to suppress WiMAX and WLAN interference. In [18], slots on the radiating patch and stepped ground structures were used to introduce WLAN band rejection. A 5.5 GHz notch was achieved in [19] using an electric LC (ELC) resonator, along with improved isolation using a grounded fractal structure. Triple-band rejection using T- and C-shaped stubs (TC-stubs) was demonstrated in [20] for WiMAX, LTE43, and WLAN bands. In [21], dual-band rejection was achieved using an SRR and an enhanced feed-line slot. Elliptical SRRs (ESRRs), a dual-via double-slot electromagnetic band gap (EBG), and a feed-line-loaded (SINR) stepped impedance resonator (SIR) are employed to reject the C-band satellite, WLAN, INSAT, and ITU bands in [22]. A U-slot-based circular patch antenna with a single band-notch was presented in [23].

As observed from the reported literature [5–23]:

- Most fabricated antennas employ complex geometrical configurations to achieve desired notch-band characteristics.
- Realization of a circular polarization band has rarely been addressed.
- Size of the antennas were not much compact.

In modern wireless communication systems, circular polarization plays a significant role in mitigating multipath fading and polarization mismatch losses, making it a preferred choice for reliable communication.

The proposed wideband-MIMO antenna is designed using a compact C-shaped radiating element excited by a tapered microstrip feedline, which effectively extends the current path and generates multiple resonant modes.

TABLE 1. Optimized design dimensions of the developed antenna element.

Parameters	L	W	L1	L2	L3	L4
Value (mm)	20	34	7	7.5	10	1.5
Parameters	L5	L6	L7	L8	W1	W2
Value (mm)	1.5	2.5	6	6	2.4	12
Parameters	W3	W4	W5	W6	W7	W8
Value (mm)	0.5	1.5	0.8	0.5	2.5	4.5
Parameters	W9	R1	R2	R3	R4	G
Value (mm)	1	3.8	4	3.5	4	23
Parameters	G1	G2	G3	G4	G5	G6
Value (mm)	10	6.5	4	6.3	6.5	0.5
Parameters	G7	G8	G9			
Value (mm)	2.5	0.3	8			

- The combined U-shaped slots and slotted ground structure introduce dual notch bands at 3.5–3.9 GHz and 5.1–5.9 GHz, while slightly extending the upper operating band.
- The antenna provides a wide circular polarization (CP) bandwidth of 6.1–7.9 GHz.
- A connected ground decoupling structure is incorporated to suppress surface-current coupling, enhancing inter-element isolation and improving overall MIMO performance.

The remainder of this paper is organized into five sections. Section 2 presents the design optimization of the two-port antenna element, including the mutual coupling reduction technique and the corresponding parametric analysis. Section 3 describes the configuration and design of the proposed four-port MIMO antenna. Section 4 provides simulated and experimental results along with validation and discussion. Finally, Section 5 concludes the study.

2. ANTENNA DESIGN

Figure 1 shows the configuration of the proposed antenna. The radiating element was excited using a $50\,\Omega$ tapered microstrip feed line to ensure effective impedance matching. The proposed antenna was designed, optimized, and simulated using Ansys HFSS (High-Frequency Structure Simulator). The antenna's optimized dimensions are listed in Table 1.

Figures 2(a)–2(c) show the design evolution of the proposed two-port element antenna, labeled as Stage-1 to Stage-3.

Stage-1:

As shown in Figure 2(a), the initial antenna configuration consists of two symmetrical C-shaped radiating elements with extended arms arranged face-to-face. The radiators are excited through tapered microstrip feed lines, while each element is backed by an independent partial ground plane optimized for impedance matching. This preliminary structure exhibits an impedance bandwidth ranging from 3.2 to 5.2 GHz, as shown in Figure 4(a).

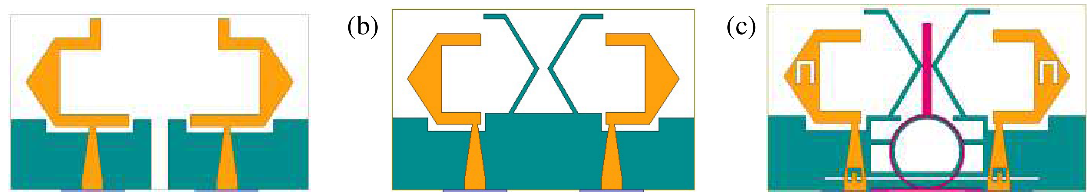

FIGURE 2. Evaluation stages of the proposed antenna. (a) Stage-1, (b) Stage-2, and (c) Stage-3.

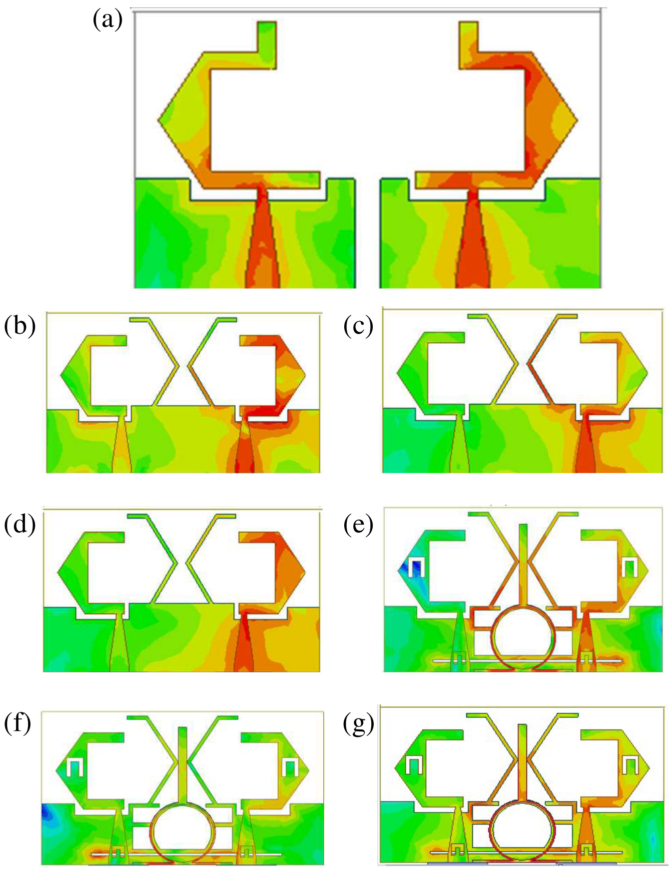

FIGURE 3. Surface current distribution at different stages: Stage-1 at (a) 4.25 GHz. Stage-2 at (b) 3 GHz, (c) 4.5 GHz, (d) 7.75 GHz. Stage-3 at (e) 3 GHz, (f) 4.5 GHz, (g) 7.75 GHz.

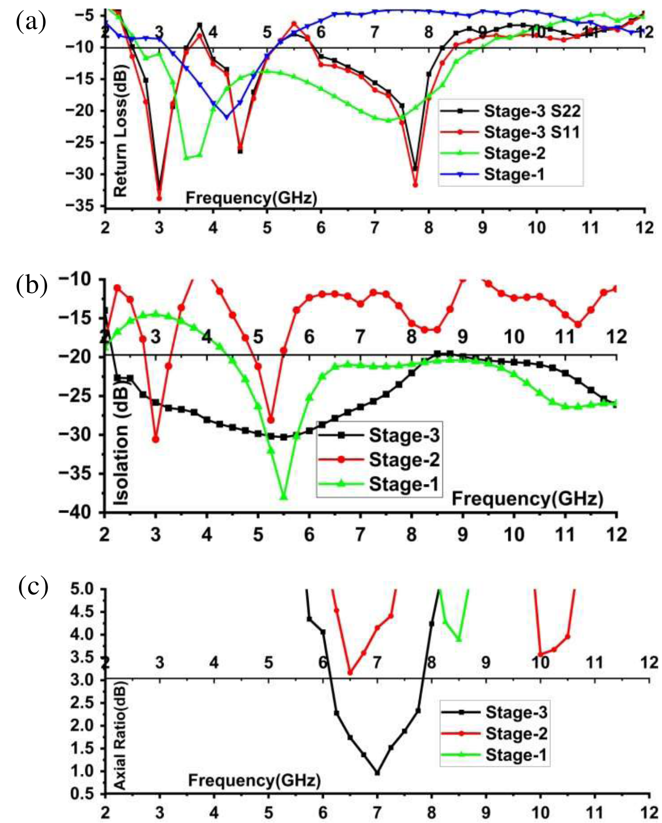

FIGURE 4. S-parameter for different stages. (a) S_{11}, (b) S_{12}, and (c) 3-dB axial ratio.

Stage-2:

The primary objective of the proposed design is to achieve wideband operation with enhanced isolation characteristics. However, the stage-1 configuration could not satisfy these requirements due to its narrow operating bandwidth and poor isolation performance. To overcome these limitations, the current distribution in stage-1 was analyzed, and structural modifications were introduced. Specifically, the two partial ground planes were interconnected using ultra-thin folded C-shaped strips, while the extended edges of the radiating patches were carefully optimized, as shown in Figure 2(b). These modifications effectively altered the current path, improving impedance characteristics and reducing undesired coupling between the antenna elements. As a result, the operating bandwidth was extended from 2.5 to 9 GHz, as illustrated in Figure 4(a), while the corresponding surface current distribution and isolation characteristics shown in Figures 3(b)–3(d) and Figure 4(b) confirm significant enhancement in inter-element isolation, particularly above 4.25 GHz.

Stage-3:

To further improve the antenna performance for practical wireless applications, the Stage-2 structure was refined to introduce band-rejection characteristics, enhance lower-band isolation, and achieve circular polarization. Based on the surface current distribution analysis, the ground plane was modified by incorporating multiple slots and an inverted C-shaped decoupling structure within the rectangular slot connecting the two ground sections. This configuration effectively controlled mutual coupling between radiating elements. Additionally, a circular ring resonator integrated with an extended parallel strip was introduced between the antenna elements, as illustrated in Figure 2(c). These modifications further enhanced isolation by effectively redistributing the surface current, as evidenced in Figures 3(e)–3(g). Consequently, the final antenna configuration achieved isolation better than -20 dB throughout the entire operating band, as shown in Figure 4(b), demonstrating its suitability for practical MIMO communication applications.

To suppress interference from coexisting wireless systems, a U-shaped slot was etched into the feed line, generating a notch band in the 3.5–3.9 GHz range for WiMAX suppression. Similarly, another U-shaped slot embedded in the radiating patch created an additional rejection band between 5.1 and 5.9 GHz to mitigate WLAN interference. Slot-loaded modifications increase the effective current path, shifting the upper cutoff frequency to 8.5 GHz. A slight variation between S_{11} and S_{22} is observed due to the influence of the common ground plane and the decoupling structure, as illustrated in Figure 4(a).

Furthermore, as illustrated in Figure 4(c), the modified structure redistributed surface currents in such a way that two orthogonal resonant modes with approximately 90° phase difference were excited. This mechanism significantly improved the axial ratio, resulting in circularly polarized radiation within the 6.1–7.9 GHz frequency band.

2.1. Parametric Tuning of the Patch Configuration

The critical design parameters (W_5, L_4, $d = R_2 - R_1$, and slot positions) affecting antenna impedance performance were systematically optimized, and the corresponding parametric analysis is illustrated in Figures 5(a)–5(e).

The feed width W_5 was varied from 0.6 mm to 1.2 mm in 0.2 mm increments. While increasing W_5 slightly affected the notch bands, the best results were achieved at $W_5 = 1$ mm, as shown in Figure 5(a). As shown in Figure 5(b), we varied L_4 from 1 mm to 2.5 mm to study its effect. Increasing L_4 influenced the resonance between the antenna ends, significantly degrading the high-frequency impedance response. The optimal result was observed at $L_4 = 1.5$ mm.

To suppress interference from existing communication systems, including WiMAX (3.3–3.7 GHz), WLAN (2.4 and 5.15–5.825 GHz), and X-band radar (8–12 GHz), while simultaneously achieving a wide circular polarization bandwidth, the radiating element was modified by incorporating U-shaped slots, complemented by multiple slots in the connected ground plane.

The dimension ($R_2 - R_1 = d$) of the inverted C-shaped structure in the ground plane significantly affects antenna isolation. A parametric study was performed for $d = 0.6$, 0.4, and 0.2 mm, and the optimized value of 0.2 mm provided the highest isolation, as shown in Figure 5(c). This optimized dimension effectively suppresses mutual coupling while preserving the desired impedance matching characteristics.

Figures 5(d) and 5(e) further demonstrate the influence of slot placement on notch bands and axial ratio characteristics. Specifically, the U-shaped slot positioned near the feed line predominantly generates notch band 1 (N_1) within 3.5–3.9 GHz and excites orthogonal resonant modes, producing circular polarization in the 6.8–7.1 GHz range. In contrast, the slot etched on the C-shaped radiating element mainly influences notch band 2 (N_2) spanning 5.1–5.9 GHz and significantly enhances circular polarization performance over 6.3–7.3 GHz by inducing stronger mode degeneration and establishing the required 90° phase difference compared to the slot placed near the feed. The simultaneous incorporation of both U-shaped slots not only realizes the intended dual band-notched characteristics but also shifts the upper cutoff frequency to 8.5 GHz and enhances the axial ratio bandwidth to 6.1–7.9 GHz, ensuring stable wideband circular polarization performance.

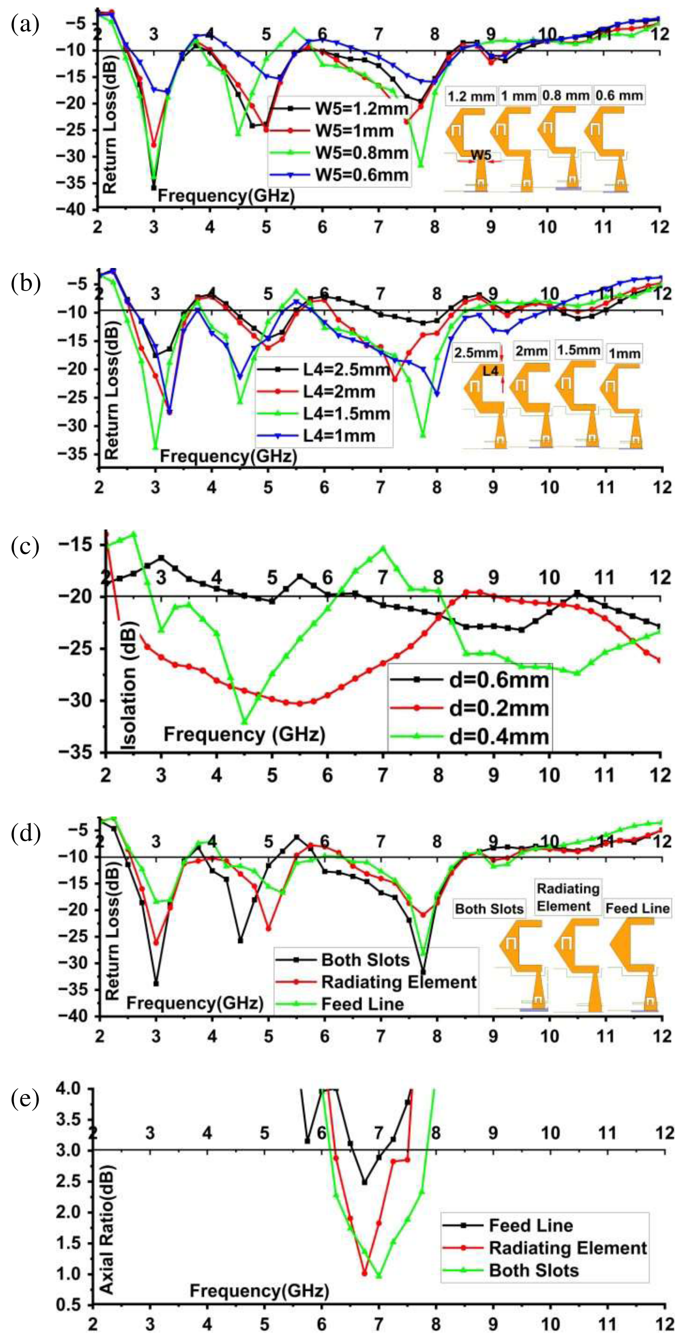

FIGURE 5. Parametric analysis of the proposed antenna: (a) variation of W_5, (b) variation of L_4, (c) isolation for different dimensions ($R_2 - R_1 = d$) of the inverted C-shaped ground ring, (d) different U-shaped slot positions, and (e) axial ratio for different U-shaped slot positions.

2.2. Equivalent Circuit

The equivalent circuit in Figure 6 illustrates the impedance behavior of the proposed antenna. The equivalent-circuit parameters for the proposed antenna were extracted using standard transmission-line and resonant-mode formulations [24–27].

For each resonant branch, the target resonant frequency f_r and quality factor Q_r are related through classical RLC reso-

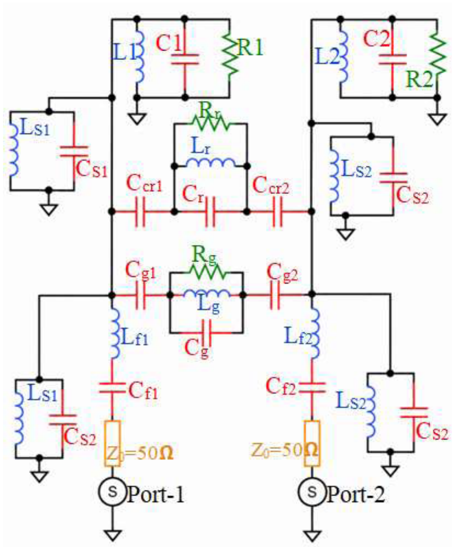

FIGURE 6. RLC equivalent circuit for the proposed design.

nance relations obtained using Equations (1) and (2):

$$f_r = \frac{1}{2\pi\sqrt{LC}} \tag{1}$$

$$Q_r = \frac{f_r}{B.W.} \tag{2}$$

As described in [24] and in RLC antenna models presented by Balanis [25] and Garg et al. [26], the modal inductance and capacitance were computed using a chosen series loss resistance $R_i \approx 50\,\Omega$, as given by Equations (3) and (4):

$$L = \frac{Q \cdot R}{W_r} \tag{3}$$

$$C = \frac{1}{W_r^2 L} \tag{4}$$

Following the S-parameter-based equivalent-circuit extraction approach of Amari et al. [27], Table 2 presents detailed description of equivalent circuit components and their corresponding values.

Figure 7 shows a comparison of S_{11} results obtained from the equivalent circuit model (ADS) shown in Figure 6 with full-wave simulated results (HFSS) presented in Figure 4(a). Reasonable agreement is observed between the two responses in resonant behavior and overall trend, with minor deviations attributed to the simplified nature of the equivalent circuit model. These deviations arise because the equivalent circuit does not fully account for distributed electromagnetic coupling and parasitic effects present in the full-wave structure. Nevertheless, the comparison confirms the validity of the proposed equivalent circuit model.

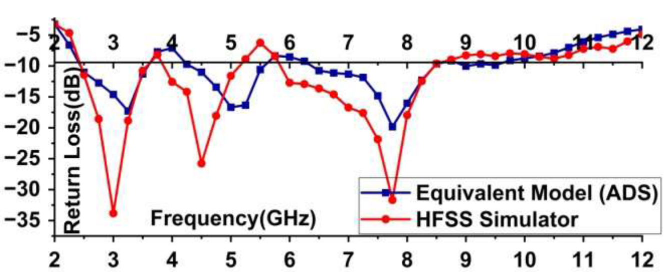

FIGURE 7. Comparison of the proposed antenna's full-wave simulation and ADS-based equivalent circuit model results.

3. FOUR PORT ANTENNA DESIGN

To enhance channel capacity in modern wireless systems, merely increasing bandwidth or transmission power is not always feasible due to spectrum scarcity and regulatory power constraints. As a practical alternative, employing multiple antennas offers a significant improvement in data throughput. Building on the initial two-port antenna design, a four-element MIMO configuration was realized by replicating the structure. This approach not only ensures adequate port-to-port isolation but also optimizes the space utilization, as shown in Figures 8(a) and 8(b).

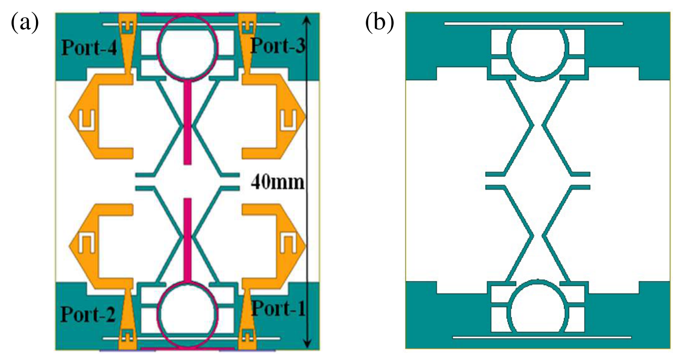

FIGURE 8. Geometry of the proposed antenna. (a) Front and (b) ground.

4. EXPERIMENTAL VALIDATION AND DISCUSSION

To validate simulated results, a prototype of the proposed dual band-rejected antenna was fabricated, as shown in Figures 9(a) and 9(b).

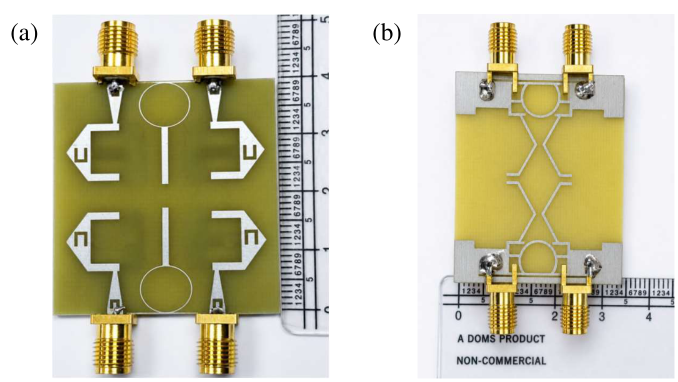

FIGURE 9. Prototype of the fabricated antenna. (a) Top view and (b) bottom view.

The fabricated antenna was characterized using a Vector Network Analyzer (Keysight N5224B PNA) to measure S-

TABLE 2. Description of equivalent circuit components.

Element	Role / Mode	Value
R1, R2	Radiation and loss resistance of the radiating patches	50 Ω
L1, L2	Equivalent inductance of the radiating patches	1 nH
C1, C2	Equivalent capacitance due to fringing electric fields of the patches	1 pF
Lf1, Lf2	Equivalent inductance of the microstrip feed lines	1 nH
Cf1, Cf2	Equivalent capacitance of the microstrip feed lines	1 pF
Rr	Loss resistance of the floating ring resonator	50 Ω
Lr	Equivalent inductance of the floating ring resonator	0.025 nH
Cr	Equivalent capacitance of the floating ring resonator	0.025 pF
Rg	Equivalent loss resistance of the defected ground resonator	50 Ω
Lg	Equivalent inductance of the defected ground resonator	0.23 nH
Cg	Equivalent capacitance of the defected ground resonator	0.23 pF
Ccr1, Ccr2	Electromagnetic coupling capacitance between the radiating patch and the floating ring resonator	0.01pF
Cg1, Cg2	Coupling capacitance between the grounds	0.03 pF
Ls1, Ls2	Slot-induced inductance	0.05 nH
Cs1, Cs2	Slot-induced capcitance	0.05 pF

(a)

(b)

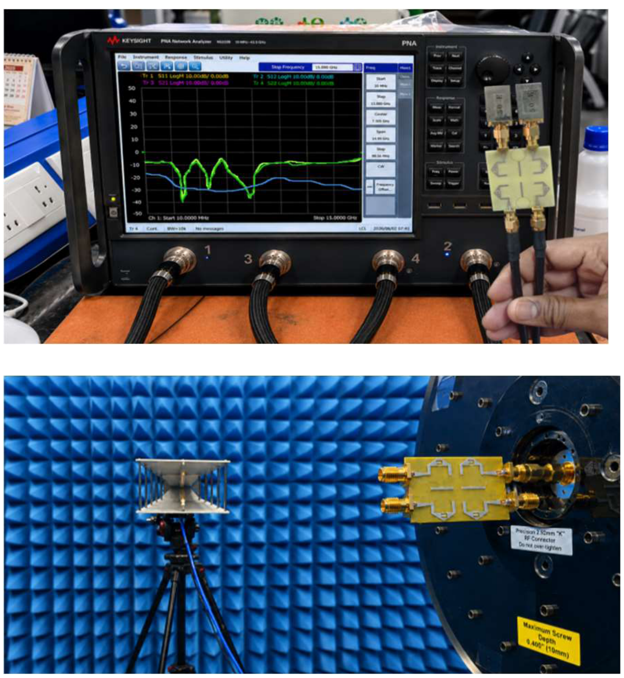

FIGURE 10. (a) Measurement setup using the Vector Network Analyzer (VNA) and (b) antenna measurement setup inside the anechoic chamber.

(a)

(b)

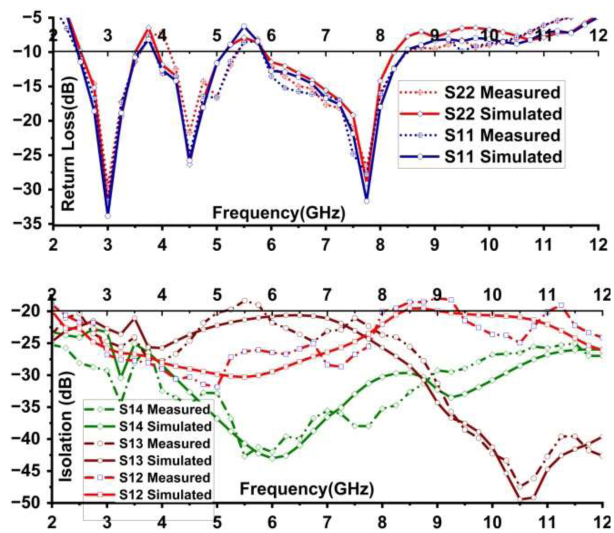

FIGURE 11. Simulated and measured. (a) Reflection coefficient and (b) isolation.

parameters, while an anechoic chamber setup was employed to evaluate its radiation characteristics, as shown in Figures 10(a) and 10(b).

4.1. S-Parameters

During S-parameter measurements, as shown in Figure 10(a), unused antenna ports were terminated with $50\,\Omega$ matched loads to accurately evaluate mutual coupling characteristics. The simulated and measured reflection coefficients (S_{11} and S_{22}), in Figure 11(a), show good agreement, confirming stable impedance matching in the operating bandwidth. As illustrated in Figure 11(b), slight deviations are observed in measured isolation parameters (S_{12}, S_{13}, and S_{14}), which can be attributed to fabrication tolerances, connector and cable losses, and external electromagnetic interference during the measurement process. Despite these minor variations, the measured isolation remains better than -20 dB across the entire operating band, demonstrating the effectiveness of the proposed MIMO antenna for the intended wireless communication applications.

4.2. Radiation Patterns

Figure 12 shows a comparison of simulated and measured co-polarization and cross-polarization radiation characteristics of the proposed antenna at resonant frequencies of 3, 5, and 7.5 GHz.

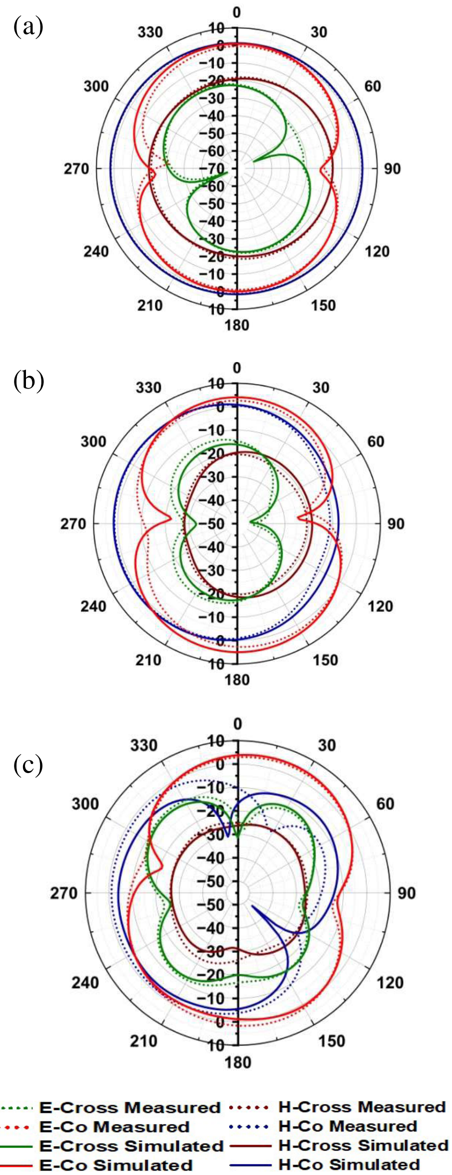

FIGURE 12. Simulated and measured E-Co, H-Co and E-Cross, H-Cross polarization patterns at (a) 3 GHz, (b) 5 GHz, and (c) 7.5 GHz.

As depicted in Figure 10(b), during radiation pattern measurements, unused ports were left open to evaluate the practical effect of mutual coupling. The measured radiation characteristics still show good agreement with the simulated results, which further validates the effective isolation performance of the proposed antenna. Since the minimum isolation between antenna elements is maintained above 20 dB, the coupled power delivered to adjacent ports is limited to approximately 1%, resulting in only negligible influence on the radiation performance.

As shown in Figure 12(a), the antenna exhibits a stable broadside radiation pattern at 3 GHz, where the co-polarized component clearly dominates over the cross-polarized field. Figure 12(b) demonstrates a similar radiation behavior at 5 GHz, although the broadside coverage is slightly reduced compared to that at 3 GHz. At 7.5 GHz, as illustrated in Figure 12(c), the antenna produces a more directional and slightly asymmetric radiation pattern due to the excitation of higher-order current modes. Nevertheless, the principal radiation characteristics are well preserved. Across all three resonant frequencies, cross-polarized components remain approximately 15–30 dB lower than corresponding co-polarized fields in the main radiation direction, indicating good polarization purity. Furthermore, the measured radiation patterns show close agreement with the simulated results, validating the radiation performance of the proposed antenna.

4.3. Axial Ratio, Peak Gain, and Radiation Efficiency

Simulated and measured axial ratio bandwidths exhibit minimal deviation across the entire circular-polarization (CP) range of 6.1–7.9 GHz, as illustrated in Figure 13(a), indicating reliable polarization performance.

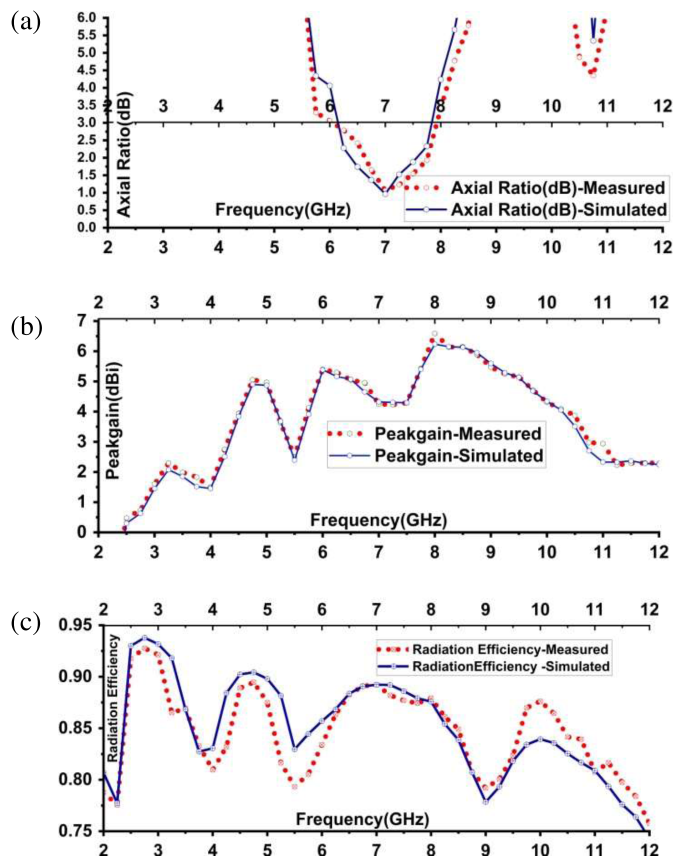

FIGURE 13. Simulated and measured. (a) Axial ratio, (b) peak gain, and (c) radiation efficiency.

As shown in Figure 13(b), the peak gain shows slight variations in the second and third operating bands (3.8–5.2 GHz and 5.8–8.5 GHz). Nonetheless, the observed gain levels are sufficient to meet the practical requirements of the intended application.

The gain performance is governed by the surface current distribution and radiation efficiency. At 3 GHz, the uniformly distributed current produces an omnidirectional radiation pattern with wider power dispersion, resulting in lower gain. As the frequency increases to 5 and 7.5 GHz, the current becomes more localized, exciting higher-order resonant modes that en-

TABLE 3. Comparative performance analysis of the proposed antenna with existing reported MIMO antenna designs.

Ref.	Antenna Size (mm^3)	N.P	Substrate	Bandwidth	Gain (dBi)	Iso (dB)	ECC	RE (%)	Pol
[8]	$30 \times 40 \times 0.8$	2	FR4	3.1–10.6 GHz	0.2–3.6	< -15	<0.15	70–77	Linear
[9]	$50 \times 40 \times 1.6$	2	FR4	2.5–11 GHz	>2.11	< -15	<0.01	47–69	Linear
[10]	$60 \times 85 \times 1.6$	2	FR4	2–9.5 GHz	1.5–5.2	< -20	<0.03	70–85	Linear
[11]	$52 \times 31 \times 1.6$	4	FR4	3.06–7.56 GHz	2–6.7	< -17	<0.05	>80	Linear
[15]	$60 \times 60 \times 0.8$	4	FR4	3.12–21.2 GHz	2–5.9	< -20	<0.04	74–92	Linear
[16]	$65 \times 65 \times 1.6$	4	FR4	2.57–11.81 GHz	1–5.8	< -20	<0.0095	78–90	Linear
[17]	$40 \times 40 \times 0.7$	2	RT-5880	3.15–11.36 GHz, N1-3.3–4 GHz, N2-4.9–5.9 GHz	3.8–5.1	< -20	<0.02	60–90	Linear
[18]	$20 \times 34 \times 1.6$	2	FR4	2.6–11.2 GHz, N1-5.2–6 GHz	2–4.1	< -20	–	61–70	Linear
[19]	$16 \times 24 \times 1.6$	2	FR4	3–12 GHz, N1-5–5.8 GHz	3–4.8	< -20	<0.01	>88	Linear
[22]	$38 \times 38 \times 0.8$	1	FR4	2.5–11 GHz, N1-3.7–4.12 GHz, N2-4.34–4.73 GHz, N3-5.43–6.25 GHz	2–4.8	–	–	–	Linear
This work	$40 \times 34 \times 1.6$	4	FR4	2.5–8.5 GHz, N1-3.5–3.9 GHz, N2-5.1–5.9 GHz	1.2–6.2	< -20	<0.05	78–90	CP 6.1–7.9 GHz

Ref: References, N.P: Number of ports, N: Notch band, Iso: Isolation, RE: Radiation efficiency, Pol: Polarization, CP: Circular polarization.

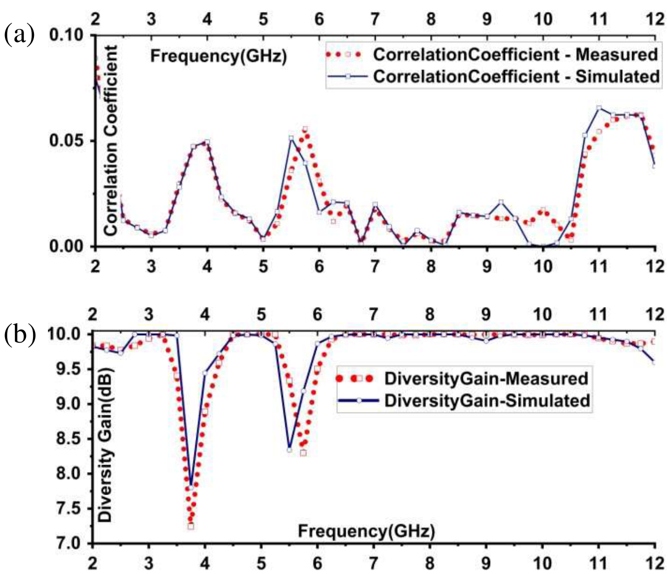

FIGURE 14. Simulated and measured. (a) Effective correlation coefficient and (b) diversity gain.

hance directivity and effective aperture, thereby improving the antenna gain despite a slight reduction in radiation efficiency.

As illustrated in Figure 13(c), the simulated radiation efficiency ranges between 80% and 90%, whereas the measured efficiency varies from 78% to 90%. Nevertheless, the antenna maintains consistently high radiation efficiency throughout the operating band, indicating stable performance and effective power utilization for wideband MIMO communication applications.

4.4. Diversity Performance Characteristics

To evaluate the diversity performance of the proposed antenna, the Envelope Correlation Coefficient (ECC) and Diversity Gain (DG) are considered critical parameters that quantify the level of signal correlation between MIMO antenna elements.

The diversity performance analysis was carried out using far-field radiation characteristics, as represented in Equations (5) and (6). This approach provides a more accurate evaluation of ECC by considering the radiation efficiency, polarization characteristics, and spatial diversity of the antenna elements, thereby offering a comprehensive assessment of MIMO system performance.

$$\text{ECC} = \frac{\left|\iint_{4\pi}[E_{\theta 1}E_{\theta 2} + E_{\phi 1}E_{\phi 2}]d\Omega\right|^2}{\left(\iint_{4\pi}(|E_{\theta 1}|^2+|E_{\phi 1}|^2)d\Omega\right)\left(\iint_{4\pi}(|E_{\theta 2}|^2+|E_{\phi 2}|^2)d\Omega\right)} \tag{5}$$

$$\text{DG} = \sqrt{1 - |\text{ECC}|^2} \tag{6}$$

As shown in Figure 14(a), both simulated and measured ECC values remain below 0.05 across the operating bands, well within the acceptable threshold for MIMO systems, indicating excellent diversity performance. Similarly, the diversity gain (DG), depicted in Figure 14(b), exceeds 9.95 across all operating frequency bands, further confirming low mutual coupling and effective spatial diversity.

4.5. Performance Comparison

Table 3 presents a detailed comparison of the proposed antenna with related existing works, considering major performance indicators, including structural dimensions, operating bandwidth, peak gain, isolation, radiation efficiency, polarization characteristics, and envelope correlation coefficient (ECC).

5. CONCLUSION

A four-element MIMO antenna system with dual-band-notched characteristics and wideband circular polarization is presented. The notched bands, designed to suppress interference from WiMAX and WLAN systems, are realized by embedding U-shaped slots in the feed line and radiating patch. These slot modifications also shift the upper cutoff frequency to 8.5 GHz and enhance the circular polarization bandwidth, resulting in stable wideband CP operation. The simulation results indicate strong isolation with mutual coupling below −20 dB, a low ECC, and radiation patterns that confirm effective diversity performance. The antenna achieves a peak gain of 6.2 dBi at 8 GHz and maintains a 3-dB axial ratio over the 6.1–7.9 GHz range. These features make the proposed antenna a promising solution for planar MIMO systems operating across the S, C, and lower X bands. Future work includes integrating metamaterial/metasurface structures for improved gain and polarization, and exploring ferrite- or graphene-based reconfigurable techniques.

REFERENCES

[1] FCC, "First Report and Order in the Matter of Revision of Part 15 of the Commission's Rules Regarding Ultra-Wideband Transmission Systems," ET-Docket 98-153, 2002.

[2] See, T. S. P. and Z. N. Chen, "An ultrawideband diversity antenna," *IEEE Transactions on Antennas and Propagation*, Vol. 57, No. 6, 1597–1605, Jun. 2009.

[3] Chandel, R., A. K. Gautam, and K. Rambabu, "Tapered fed compact UWB MIMO-diversity antenna with dual band-notched characteristics," *IEEE Transactions on Antennas and Propagation*, Vol. 66, No. 4, 1677–1684, Apr. 2018.

[4] Ko, S. C. K. and R. D. Murch, "Compact integrated diversity antenna for wireless communications," *IEEE Transactions on Antennas and Propagation*, Vol. 49, No. 6, 954–960, Jun. 2001.

[5] Ismail, N. and E. A. Kadir, "A co-planar waveguide ultrawideband antenna for ambient Wi-Fi RF power transmission and energy harvesting applications," *International Journal of Engineering and Technology Innovation*, Vol. 13, No. 4, 265–283, 2023.

[6] Pandey, U., P. Singh, R. Singh, V. Kumar, K. Ray, S. Mallik, H. M. Alshahrani, E. Elshiekh, M. Abbas, and B. O. Soufiene, "Ultra-wideband microstrip folded antenna for wireless LAN, 5G and Internet of Things applications," *Scientific Reports*, Vol. 14, No. 1, 29319, 2024.

[7] Nie, N.-S., X.-S. Yang, and B.-Z. Wang, "A compact four-element multiple-input-multiple-output antenna with enhanced gain and bandwidth," *Microwave and Optical Technology Letters*, Vol. 61, No. 7, 1828–1834, 2019.

[8] Deng, J.-Y., L.-X. Guo, and X.-L. Liu, "An ultrawideband MIMO antenna with a high isolation," *IEEE Antennas and Wireless Propagation Letters*, Vol. 15, 182–185, 2016.

[9] Lin, G.-S., C.-H. Sung, J.-L. Chen, L.-S. Chen, and M.-P. Houng, "Isolation improvement in UWB MIMO antenna system using carbon black film," *IEEE Antennas and Wireless Propagation Letters*, Vol. 16, 222–225, 2017.

[10] Zhao, X., S. P. Yeo, and L. C. Ong, "Planar UWB MIMO antenna with pattern diversity and isolation improvement for mobile platform based on the theory of characteristic modes," *IEEE Transactions on Antennas and Propagation*, Vol. 66, No. 1, 420–425, Jan. 2018.

[11] Nirmal, S., S. Kumar, and R. Chandel, "Quad-port staircase U-shaped wideband MIMO antenna for 5G new radio applications," *Progress In Electromagnetics Research Letters*, Vol. 125, 43–50, 2025.

[12] Ali, W. and M. A. Azeem, "Dual band Notched 2-port UWB MIMO antenna reconfiguration using lumped capacitors," *Scientific Reports*, Vol. 16, No. 1, 5265, 2026.

[13] Saraswat, R. K. and M. Kumar, "A vertex-fed hexa-band frequency reconfigurable antenna for wireless applications," *International Journal of RF and Microwave Computer-Aided Engineering*, Vol. 29, No. 10, e21893, 2019.

[14] Mallani, H., A. Agrawal, and R. K. Saraswat, "Implementation of fractal metamaterial inspired antenna for multi-standard wireless applications," *Progress In Electromagnetics Research B*, Vol. 108, 121–137, 2024.

[15] Ji, L., C. Du, Y. Yang, and F. Zhang, "Characteristic mode-inspired ultra-wideband dual-band notched four-port MIMO antenna," *Progress In Electromagnetics Research C*, Vol. 171, 75–86, 2026.

[16] Wang, Z., Z. Wang, W. Nie, and H. Lin, "A compact ultra-wideband MIMO antenna with triple band-notched characteristics," *Progress In Electromagnetics Research C*, Vol. 169, 279–289, 2026.

[17] Dhasarathan, V., T. K. Nguyen, M. Sharma, S. K. Patel, S. K. Mittal, and M. T. Pandian, "Design, analysis and characterization of four port multiple-input-multiple-output UWB-X band antenna with band rejection ability for wireless network applications," *Wireless Networks*, Vol. 26, No. 6, 4287–4302, 2020.

[18] Hatami, N., J. Nourinia, C. Ghobadi, M. Majidzadeh, and B. Azarm, "High inter-element isolation and WLAN filtering mechanism: A compact MIMO antenna scheme," *AEU — International Journal of Electronics and Communications*, Vol. 109, 43–54, 2019.

[19] Gorai, A. and R. Ghatak, "Utilization of shorted fractal resonator topology for high isolation and ELC resonator for band suppression in compact MIMO UWB antenna," *AEU — International Journal of Electronics and Communications*, Vol. 113, 152978, 2020.

[20] Sharma, M., V. Dhasarathan, S. K. Patel, and T. K. Nguyen, "An ultra-compact four-port 4×4 superwideband mimo antenna including mitigation of dual notched bands characteristics designed for wireless network applications," *AEU — International Journal of Electronics and Communications*, Vol. 123, 153332, 2020.

[21] Abdpour, S. S., N. Azadi-Tinat, H. Oraizi, and J. Ghalibafan, "Design of WLAN/WiMAX band notch super-wideband microstrip fractal antennas," *International Journal of Microwave and Wireless Technologies*, Vol. 11, No. 8, 844–850, 2019.

[22] Arora, S., S. Sharma, and R. Anand, "Ultra-wideband antenna with quintuple band notches integrated with metamaterials," *Progress In Electromagnetics Research M*, Vol. 122, 41–52, 2023.

[23] Singh, K. and R. Mishra, "Design of a circular microstrip patch antenna with single band notch characteristic for UWB applications," in *2017 IEEE International WIE Conference on Electrical and Computer Engineering (WIECON-ECE)*, 262–265, Dehradun, India, 2017.

[24] Pozar, D. M., *Microwave Engineering*, 4th ed., Wiley, 2011.

[25] Balanis, C. A., *Antenna Theory: Analysis and Design*, 4th ed., Wiley, 2016.

[26] Garg, R., P. Bhartia, I. Bahl, and A. Ittipiboon, *Microstrip Antenna Design Handbook*, Artech House, 2001.

[27] Amari, S., U. Rosenberg, and J. Bornemann, "Adaptive synthesis and design of resonator filters with source/load-multiresonator coupling," *IEEE Transactions on Microwave Theory and Techniques*, Vol. 50, No. 8, 1969–1978, Aug. 2002.